

PAPER

View Article Online
View Journal | View IssueCite this: *J. Mater. Chem. A*, 2018, 6,
7827

卷(期)(年): 2018, 6

用于析氢反应的Ni₃P 表面和界面性质的理论研究A theoretical study on the surface and interfacial
properties of Ni₃P for the hydrogen evolution
reaction†Jun Hu, ^{ab} Shunli Zheng,^a Xin Zhao, ^{a*}  姚昕^a and Zhong Chen ^{a*}

We report a comprehensive density functional theory (DFT) study on the stability, geometric structure, electronic characteristics, and catalytic activity for the hydrogen evolution reaction (HER) on low-index Ni₃P crystal surfaces, namely, the (001), (100), (110), (101) and (111) planes with different surface terminations. The results indicate that P-rich and some stoichiometric surfaces are thermodynamically stable. Eight stable surfaces were selected to investigate the electronic characteristics and catalytic activity. The (110)B facet of Ni₃P is indispensable for the HER, because it not only displays improved electrocatalytic activity, but also possesses suitable potential and high stability. Increasing the active sites through doping or enlarging the surface area could be a useful strategy to improve the HER activity further. Furthermore, it was found that Ni₃P requires higher energies for decomposition in the absence of O₂, although it is thermodynamically unstable in aqueous solutions with most pH values and potentials. This study provides important insights into the surface properties of Ni₃P for water splitting and opens up an exciting opportunity to optimize the performance of solar energy conversion devices by synthesizing preferentially exposed catalyst facets.

Received 14th January 2018
Accepted 27th March 2018

DOI: 10.1039/c8ta00437d

rsc.li/materials-a

Introduction

The hydrogen evolution reaction (HER) by using electrochemical water splitting has long been considered as an important technology without any environmental pollution.¹ Among the cathode materials for water splitting, including transition metals and their dichalcogenides,^{2–5} carbides,^{6,7} borides,⁸ and nitrides,⁹ phosphides have attracted considerable attention in the field of electrochemical catalysis due to their many advantages such as earth-abundance, high catalytic activity, good stability and facile synthesis.^{10,11} Nickel phosphide (Ni_xP_y) is one of the most promising candidates among transition metal phosphides. In these types of compounds, phosphorus has a lower catenation tendency and exhibits a wide variety of building blocks (cages, dumbbells, etc.) and superstructures (1D to 3D chains). Furthermore, Ni_xP_y often forms amorphous films which are immune to chemical attack at grain boundaries, and therefore they generally possess high corrosion resistance in acidic solutions and can only be dissolved in hot oxidising acids such as HNO₃.¹² Nickel phosphides have been reported in more than ten stoichiometric compositions,^{13–16}

among which Ni₁₂P₅, Ni₂P, Ni₅P₄, and NiP₂ have attracted much attention for their synthesis, structure, and reactivity.^{17–19}

Ni₃P, as the most Ni rich phosphide, has been mostly reported for its roles at the solder joint interface formed by reaction-induced crystallization. It has been reported that Ni₃P can also be synthesized using electrochemical deposition,^{20,21} solid state reactions²² and hydrothermal reactions.^{23,24} However, a few Ni rich phosphides are reported as the electro-cathode materials for hydrogen evolution.²⁵ Recently, Jin *et al.* reported the HER properties of trinickel monophosphide (Ni₃P) porous hollow nanospheres, which showed efficient catalytic performance. The overpotential required to reach a current density of 20 mA cm^{−2} is as small as 99 mV in an acidic solution.²⁶ Pan *et al.* investigated the electrocatalytic properties for the HER of different types of nickel phosphides (Ni₁₂P₅, Ni₂P and Ni₅P₄) and found that the catalytic properties followed the order of Ni₅P₄ > Ni₂P > Ni₁₂P₅, and their potentials at a current density of 10 mA cm^{−2} are 118, 137 and 208 mV, respectively.¹⁸ It was suggested that the Ni-rich phosphide has a relatively poor HER activity. However, Ni₃P, as the most Ni rich phosphide, was found to be more active in the experiment.²⁶ The difference among the few existing reports indicates that it is crucial to obtain a comprehensive understanding of Ni₃P for its roles in the HER. Recently, *in situ* experimental results of most catalysts show that facet orientations play crucial roles on catalytic activity.^{27–32} These results show that facet orientation is an important consideration for the design and fabrication of highly efficient catalysts. However, among the theoretical

^aSchool of Materials Science and Engineering, Nanyang Technological University, 50 Nanyang Avenue, Singapore 639798. E-mail: xinzhaoh@ntu.edu.sg; ASZChen@ntu.edu.sg

^bSchool of Chemical Engineering, Northwest University, Xi'an, P. R. China 710069

† Electronic supplementary information (ESI) available. See DOI: 10.1039/c8ta00437d

studies, most researchers only paid attention to the stoichiometric surface to understand the surface properties and reaction mechanism.³³ The non-stoichiometric surface could be more stable in most cases, and could truly represent the reality.³⁴ Therefore, attention should also be paid to non-stoichiometric surfaces during theoretical studies.

In this work, we report a comprehensive theoretical study of Ni_3P , including its geometric structure, electronic characteristics, HER activity and stability for different surface orientations and terminations using density functional theory (DFT) calculations. Our current study provides an improved understanding of this material and insights into its electro-catalytic ability for the HER. The outcome also helps in the design and selection of electrocatalysts in the experiment.

Results and discussion

Surface energies for different ordinations and terminations

Surface energy is an important parameter that affects the stability and catalytic activity. Fig. 1 shows the surface energies of stable surfaces with different terminations.

At first, the allowed ranges of chemical potentials ($\Delta\mu_{\text{P}}$, $\Delta\mu_{\text{Ni}}$) were determined from the formation energy of different structures. The results of Fig. 1(a) are consistent with previous experiments and calculations.^{35–37} We find that Ni_3P is stable at $-1.78 \text{ eV} < \Delta\mu_{\text{P}} < -1.18 \text{ eV}$. When $\Delta\mu_{\text{P}}$ is smaller than -1.78 eV , bulk Ni becomes thermodynamically favorable, while Ni_{12}P_5 becomes favorable when $\Delta\mu_{\text{P}}$ is larger than -1.18 eV . Considering the temperature effect and interface reorganization contributions, the $\Delta\mu_{\text{P}}$ was enlarged from -1.88 eV to -1.08 eV during the surface energy calculation. Fig. 1(b) demonstrates the stable terminations for different low-index surfaces. It indicates that Ni-rich surfaces are not stable in all low-index surfaces as there is no line with a slope greater than zero. For the (001) and (011) surfaces, the P-rich surfaces are stable in the whole region of $\Delta\mu_{\text{P}}$. For the (110) and (111) surfaces, the P-rich surfaces are stable in a large region especially in the P-rich

environment ($\Delta\mu_{\text{P}}$ around -1.18 eV), while stoichiometric surfaces become stable in the Ni-rich environment ($\Delta\mu_{\text{P}}$ around -1.78 eV). For the (100) surface, stoichiometric surfaces are stable in a large region. Furthermore, the (110) surface has the lowest surface energy. Based on the surface energies, the above eight surfaces with the lowest energies were selected to investigate the electronic characteristics and catalytic activity.

Geometric structure of stable surfaces

The optimized geometric structures of eight stable surfaces are shown in Fig. 2.

Fig. 2 displays the top and side views of stable surfaces with different terminations. Among these surfaces, the (100)B, (110)C and (111)D are the stoichiometric surfaces while others are P-rich surfaces. In all surfaces, the surface Ni and P atoms are coplanar in a relaxed slab. Comparing the relaxed surface with the unrelaxed surface, it was found that the surface P and Ni atoms move inward slightly, making them coplanar on the surface. The change in the surface bonding configuration is caused by minimization of the system energy.

Electronic characteristics of stable surfaces

To reveal the origin of HER activity of Ni_3P , the Density of States (DOS) of bulk Ni_3P and the low-index surfaces are calculated as shown in Fig. 3. In order to find the change of the electronic structure, the electronic structures of black P and bulk Ni are also added and compared with that of Ni_3P .

As illustrated in Fig. 3(a), we found that the carrier density of Ni_3P changes greatly when compared with black P and Ni metal. The electrons of black P are not localized while the electrons of bulk Ni_3P are localized, indicating that the bond energy of Ni_3P is greatly increased compared to that of black P. Furthermore, there are strong and broad peaks ranging from -5 to 2 eV for metal Ni while the range and intensity of the peaks reduced especially near the Fermi energy for bulk Ni_3P , which indicates that the free carrier density of Ni_3P under the Fermi level is

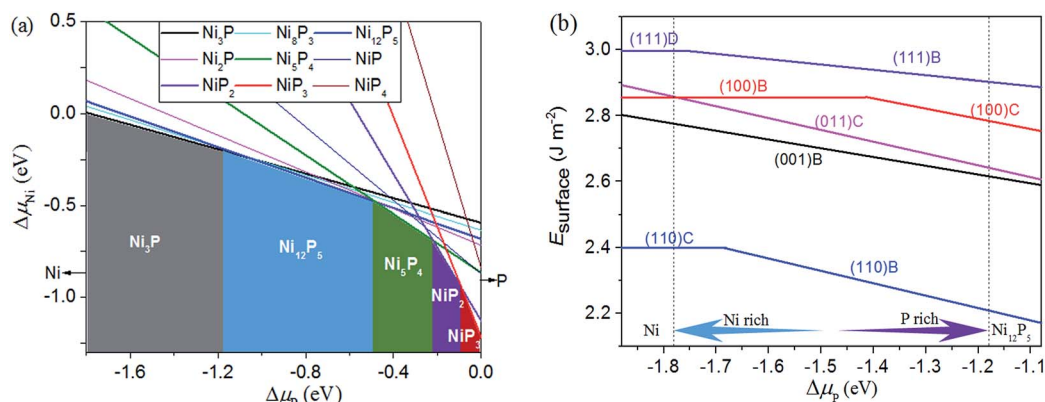


Fig. 1 (a) Bulk phase diagram as a function of the relative chemical potentials (eV) of Ni and P for nickel phosphide phases. Each solid line satisfies the equilibrium equation: $\Delta G_{\text{Ni}_x\text{P}_y} = x\Delta\mu_{\text{Ni}} + y\Delta\mu_{\text{P}}$ at 0 K. The regions of thermodynamic stability for Ni_xP_y are indicated with color. (b) The surface energies of stable surfaces with different terminations. A, B, C and D stand for different terminations, where lines parallel to the x axis stand for stoichiometric surfaces and lines with negative slopes stand for P-rich surfaces. More details about the positions of terminations can be found in ESI, Fig. S1.† Details about the surface energies of considered surfaces can be found in ESI Table S1 and Fig. S2.†

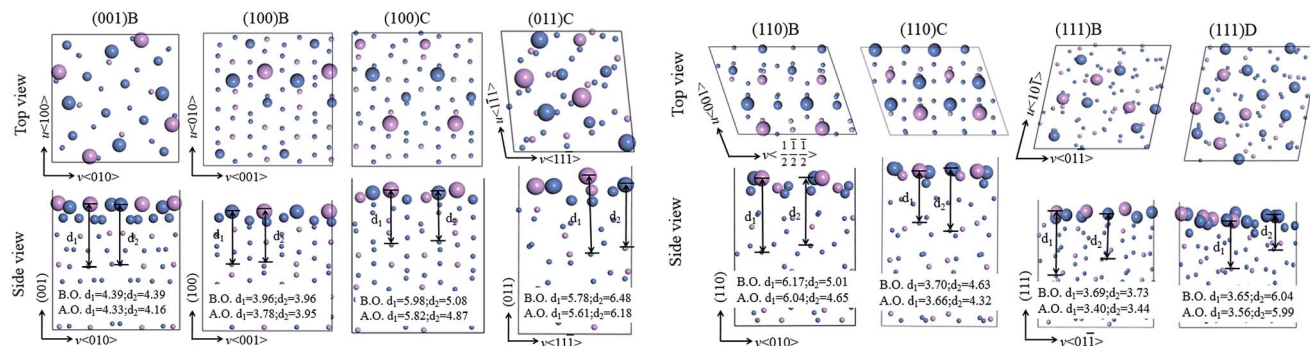


Fig. 2 The optimized geometric structures of eight stable surfaces, where surface vectors are also indicated. The atoms in the first layer of the surface are shown in big spheres, those in the second layer of the surface are shown in medium-sized spheres and the others are shown in small spheres. Violet spheres stand for P atoms and blue spheres stand for Ni atoms. B.O. stands for the geometric structure before optimization while A.O. stands for the geometric structure after optimization. d_1 and d_2 stand for the distance of the two atoms as labeled.

reduced.³⁸ It can be observed from Fig. 3(b) that the DOS in the region of -5 eV to -4 eV is greatly increased for all of those surfaces when compared with bulk Ni_3P . This is consistent with

the above geometric structure where surface P moves inward and the bond energy increases. On the surfaces, the DOS near the Fermi energy will slightly increase due to disappearance of

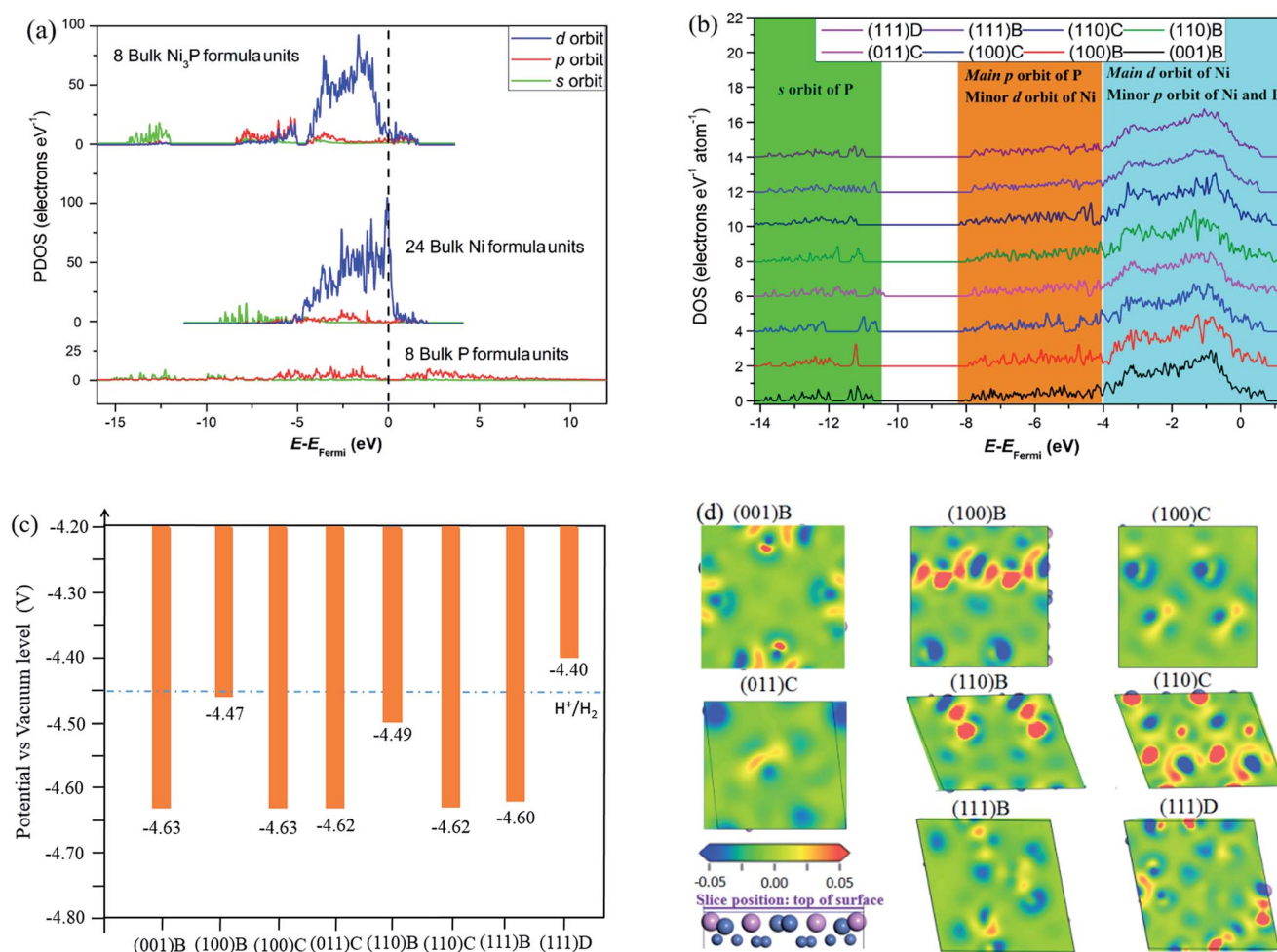


Fig. 3 The calculated electronic characteristics of bulk Ni_3P and its low-index surfaces. (a) Density of States (DOS) of black P, metallic Ni, and Ni_3P ; (b) Density of States (DOS) of one atom on the (001)B, (100)B, (100)C, (011)C, (110)B, (110)C, (111)B and (111)D; (c) potentials of different low-index surfaces; (d) electron density difference map of different low-index surfaces; a loss of electrons is indicated in blue while electron enrichment is indicated in red.

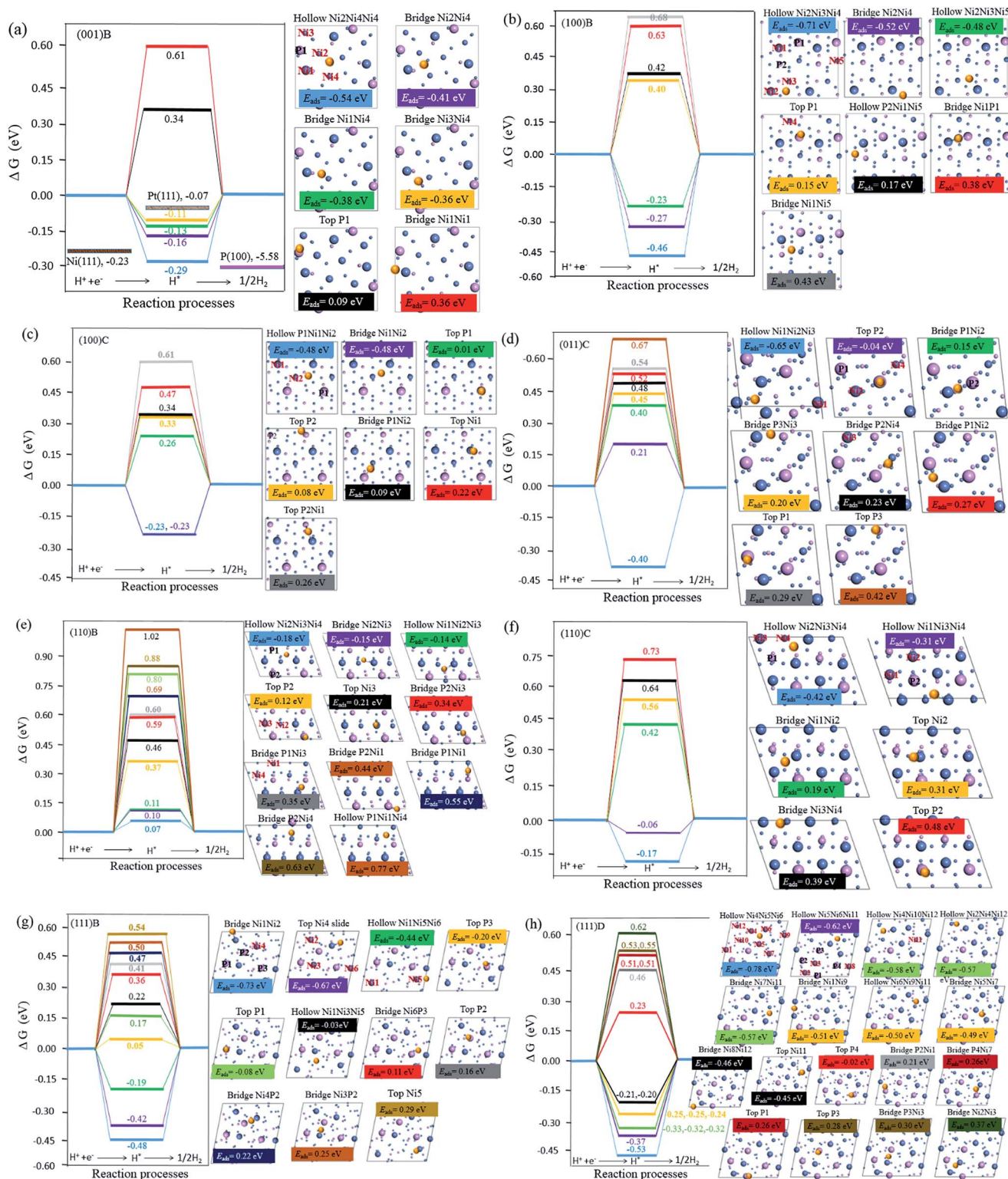


Fig. 4 Free energy profiles of H_2 generation on different active sites of surfaces. (a) The (001)B surface with Pt(111) and Ni(111) surfaces for comparison; (b) the (100)B surface; (c) the (100)C surface; (d) the (011)C surface; (e) the (110)B surface; (f) the (110)C surface; (g) the (111)B surface; and (h) the (111)D surface. Yellow spheres stand for H atoms, violet spheres stand for P atoms and blue spheres stand for Ni atoms. More details about adsorption sites can be found in ESI, Fig. S5–S12 and Tables S2–S9.†

the anti-bond, compared with bulk Ni_3P . Based on Fig. S3,† the main contributions for the Fermi energy are from Ni 3d, and some from Ni 4p and P 3p. A significant overlap of states from

–8 eV to –5 eV is mainly due to the interaction between Ni 3d and P 3p orbitals; the formation of Ni–P bonds produces a weak ligand effect by minor stabilization of the Ni 3d levels and

a small Ni to P charge transfer.³⁹ To better understand the ability of different surfaces for photocatalytic applications towards water splitting, the positions of the Fermi energies of different facets are investigated by work function calculations as indicated in Fig. S4.† Fig. 3(c) shows that the biggest potential difference between the surfaces and the HER is only 0.18 V, although the potentials for most surfaces are more negative than that of the HER. This indicates that all of the surfaces are suitable for the HER, especially the (100)B, (110)B and (111)D surfaces based on Fermi energy consideration. As shown in Fig. 3(d), the bridge of Ni–P is electron enriched and top Ni easily loses electrons.

The surface activity for the HER

To understand the origin of the catalytic activity of different facets in the HER, DFT calculations of the Gibbs free energies of hydrogen adsorption were carried out. As the adsorption free energy of hydrogen (ΔG_{H}) has been shown to be a good descriptor of materials for catalyzing hydrogen generation following either the Volmer–Tafel or the Heyrovsky mechanism,⁴⁰ ΔG_{H} was used in this work to evaluate the catalytic activity of catalysts for the HER. In principle, the catalytic activity of a catalyst correlates with the ΔG_{H} value, a smaller ΔG_{H} (absolute value) indicating better HER activity.⁴¹

Fig. 4 displays the calculated free energy diagram for hydrogen evolution on different active surface sites. As illustrated in Fig. 4(a), we found that free energies for hydrogen evolution are -0.23 eV and -0.07 eV for Ni(111) and Pt(111) surfaces, respectively, and this is largely consistent with previous experimental and calculated results.^{42,43} Furthermore, it is observed that the hollow Ni site is the most stable site for adsorption of the H atom. However, most of those stable adsorption sites are not catalytically active because it requires a high energy for desorption of the adsorbed H^* (bond-breaking

processes).⁴⁴ Taking (001)B as an example, the most stable adsorption positions are the hollow sites of $\text{Ni}_2\text{Ni}_4\text{Ni}_4$ with an adsorption energy of -0.54 eV. This is also consistent with previous findings, where the unsaturated species prefer the bridge or hollow sites.⁴⁵ The bridge Ni_1Ni_4 , bridge Ni_3Ni_4 , and top P1 sites are able to trap protons and bond the atomic hydrogen while still desorb H_2 easily. This agrees well with the results reported by Jin and coauthors.²⁶ It is notable that the stable adsorption site is also the active site for the (110)B facet with a free energy of 0.07 eV. This is important for the HER. When the active site is the stable site, H^* will be supplied continuously because it is the most energetically favorable to adsorb the H atom for the active site. However, when the stable adsorbed H^* is not the active site as other surfaces, the H^* will be firstly adsorbed on the stable site and then on the active site. The first adsorbed H^* may induce the charge redistribution and then affect the HER activity. Fig. 5 is a summary of the exchange current for hydrogen evolution and density of active sites on different Ni_3P surfaces.

As indicated in Fig. 5, the over-potentials on the (111)B, (110)B and (110)C for the HER is 0.05 V, 0.07 V and 0.06 V, which are even better than that of Pt(111). These three surfaces could be the ideal surfaces for the HER. However, the largest number of active sites is only $0.036 \text{ N } \text{\AA}^{-2}$ on the (110)B and (110)C surfaces under applied 100 mV over-potential. This is much small than that of the Pt(111) surface (nearly $0.132 \text{ N } \text{\AA}^{-2}$). Increasing the active sites by doping or enlarging the specific surface area by nanostructure formation could be a useful strategy to improve the HER activity of Ni_3P further.

Chemical stability of low-index surfaces

The resistance against chemical degradation is an important consideration for the electrode material for electrochemical catalytic reactions. Pourbaix diagrams can assess the stability

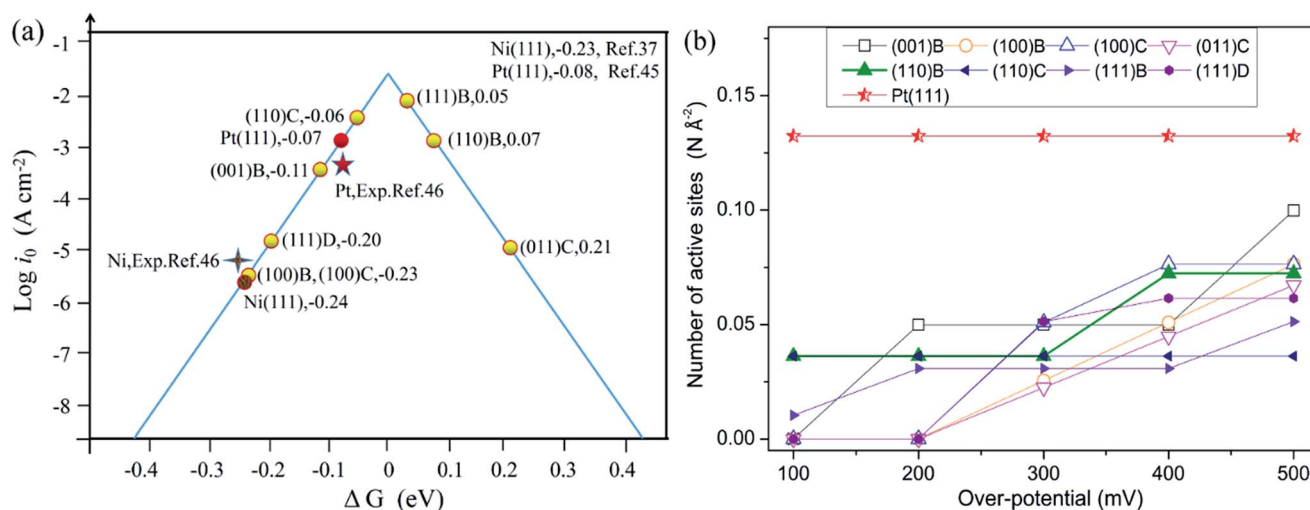


Fig. 5 (a) The exchange current for hydrogen evolution over different Ni_3P surfaces, Pt(111) and Ni(111) plotted as a function of the calculated hydrogen chemisorption energy. The experimental data for Ni and Pt from ref. 44 are also added; (b) the number of active sites on different surfaces, double counting is to be avoided. Take the (001)B for example, both the hollow $\text{Ni}_2\text{Ni}_4\text{Ni}_4$ site and bridge Ni_2Ni_4 site can absorb the H atom; these two sites can only be counted once because they refer to the same atom.

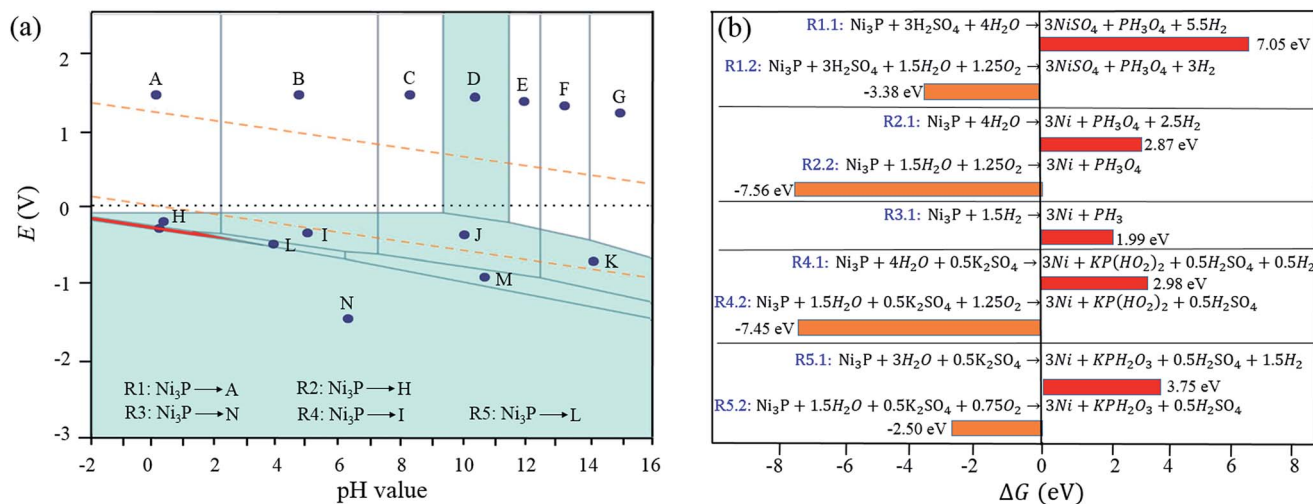


Fig. 6 Evaluation of stability by computational methods. (a) The Pourbaix diagram of the 75–25% Ni–P system in aqueous solution, assuming a Ni ion concentration of 10^{-6} mol kg⁻¹ and a P ion concentration of 10^{-6} mol kg⁻¹. The red region represents Ni₃P. Other regions are labelled for stable phase(s) of: (A) Ni²⁺ + H₃PO₄(aq); (B) Ni²⁺ + H₂PO₄⁻; (C) Ni²⁺ + HPO₄²⁻; (D) NiO(s) + PO₄³⁻; (E) Ni(OH)₃⁻ + HPO₄²⁻; (F) Ni(OH)₃⁻ + PO₄³⁻; (G) Ni(OH)₄²⁻ + PO₄³⁻; (H) Ni(s) + H₃PO₄(aq); (I) Ni(s) + H₂PO₄⁻; (J) Ni(s) + HPO₄²⁻; (K) Ni(s) + HPO₄²⁻; (L) Ni(s) + H₂PO₃⁻; (M) Ni(s) + HPO₃²⁻; and (N) Ni(s) + PH₃(aq); upper and down dash lines stand for the equilibrium potential of O₂/H₂O and H⁺/H₂. The related reactions are also indicated. (b) The calculated ΔG for the possible decomposition process of Ni₃P with and without O₂.

against decomposition into any combination of solids.⁴⁶ We have calculated the Pourbaix diagram of Ni–P and the Gibbs energies for the corresponding decomposition process, as shown in Fig. 6(a).

Thermodynamically, Ni₃P is stable only in a small region with pH values from -2 to 3 and at the narrow electrochemical potential window below $\phi(\text{H}^+/\text{H}_2)$. From the thermodynamic perspective, Ni₃P may transform into Ni(s) and Ni²⁺ with chemical reactions R1–R5 in aqueous solutions. We choose H₂SO₄, H₂O, H₂, and K₂SO₄ in the calculation as they are commonly encountered environments by an HER electrode. The ΔG for the above possible processes of Ni₃P degradation is shown in Fig. 6(b). As indicated in Fig. 6(b), the ΔG for the decomposition of Ni₃P is negative in the presence of O₂ while positive without the presence of O₂ for these selected degradation processes. Therefore, Ni₃P can be thermodynamically stable in solutions without the presence of O₂. However, in the presence of O₂, Ni₃P has a tendency to corrode. Besides the thermodynamic consideration, the stability of Ni₃P in a practical situation also depends on the kinetic process, because any reaction would require additional energy for structural rearrangement. Based on the above analysis, we confirm that Ni₃P can be stable without strongly oxidative conditions in typical HER solutions. Therefore, Ni₃P can only be used as a cathode material for water splitting (as the anode surface will generate reactive oxygen species). In an experimental setup, it is necessary to reduce the O₂ concentration in the solution. To verify our prediction, an experiment was carried out where flowing O₂ gas through the solution reduced the current density quickly while flowing Ar increased the current density gradually (in ESI, Fig. S13†).

Conclusions

In this paper, a comprehensive theoretical analysis was carried out on the geometric structure, electronic characteristics, HER activity and stability of different Ni₃P surfaces with different terminations. The results indicate that P-rich and some stoichiometric surfaces are thermodynamically stable. Eight such stable low-index surfaces with different surface terminations were then selected to investigate their electronic characteristics and catalytic activity. It is demonstrated that most of the stable adsorption sites are not catalytically active because a high energy is required for desorption of the adsorbed H*. Among the stable low-index surfaces, the (110)B has a low over-potential and more active site density for the HER by electrochemical catalysis. The (110)B surface is also the most stable surface which should be easily synthesized in the experiment. It is hereby shown that the (110)B surface in Ni₃P is indispensable for the HER, because of its good electrocatalytic activity, suitable potential, and high stability. Although the over-potential of (110)B is close to that of Pt, the number of active sites for (110)B is only 27% of the one on Pt(111). Increasing the active sites through doping or enlarging the surface area by nanostructure formation could be a useful strategy to improve the HER activity of Ni₃P further. Furthermore, Ni₃P needs more energy in its decomposition process without O₂ although it is thermodynamically unstable in most aqueous solutions according to the Pourbaix diagram. O₂ was found unfavorable for the stability of Ni₃P. Thus, it is necessary to reduce O₂ during the electrochemical catalysis process. Our study has provided insights into the properties of Ni₃P facets. The obtained understandings are useful for the design and fabrication of cathode materials for solar energy conversion devices.

Computational methods

The CASTEP module of Materials Studio software (Accelrys Inc.) was employed for the quantum chemistry calculations. The surfaces were obtained from the optimized Ni₃P (space group 82) with a vacuum region of 15 Å. During the calculations, self-consistent periodic DFT was adopted to explore the electronic structure and catalytic activities on the facets. Ionic cores were represented by an ultrasoft pseudopotential. Perdew–Burke–Ernzerhof (PBE) approximation was selected as the Generalized Gradient Approximation (GGA) method to calculate the exchange–correlation energy. The Broyden–Fletcher–Goldfarb–Shanno (BFGS) scheme was selected as the minimization algorithm. DFT-D correction was used for dispersion corrections. The energy cutoff is 380 eV and the SCF tolerance is 1.0×10^{-6} eV per atom. The optimization is completed when the energy, maximum force, maximum stress and maximum displacement are smaller than 5.0×10^{-6} eV per atom, 0.01 eV Å⁻¹, 0.02 GPa and 5.0×10^{-4} Å, respectively.⁴⁷ The *k*-point samplings were set as $2 \times 2 \times 3$ for the bulk and $2 \times 2 \times 1$ for surfaces during the calculations because there is no significant change in the calculated energies for a larger *k*-point mesh. Furthermore, at least five P layers were selected to reduce the dispersive error (see Fig. S14†). Considering the symmetry of the (001), (100), (110), (101) and (111) surfaces with different terminations, 19 surfaces were chosen for the calculation (see ESI, Fig. S1 and S15†). The calculated crystallographic parameters are in good agreement with experimental data, as listed in Table S10.† Table S11† shows the calculated energies of related species during calculation. The surface energy can be calculated using eqn (1). The formation energies for Ni₃P are indicated as eqn (2):

When adding eqn (2) and eqn (1), we can obtain the surface energy as eqn (3), where E_{slab} is the total energy of the slab model, $E_{\text{bulk Ni}}$ and $E_{\text{bulk P}}$ are the total energy per atom of the metal Ni fcc and black P, n_{Ni} and n_{P} are the number of atoms that the slab model contains, and A is the surface area of the slab model. The free energy of the adsorption atomic hydrogen is obtained using eqn (4), where ΔE_{ZPE} denotes the zero-point energy of the system and is simplified as 0.05 eV. The term $-T\Delta S_{\text{H}}$ is the contribution from entropy at temperature *K* and is 0.20 eV at 298 K.⁴⁸ ΔE_{H} describes the energy needed to increase the coverage by one hydrogen atom, which is calculated as eqn (5), where $E[\text{Ni}_3\text{P} + \text{H}]$ is the total energy of the system, including the adsorbed molecules and the Ni₃P facet; $E[\text{Ni}_3\text{P}]$ is the energy of the Ni₃P facet; $E(\text{H}_2)$ represents the total energy of a gas phase H₂ molecule. The exchange current at pH 0 can be calculated using eqn (6) and (7),⁴² where k_0 is the rate constant, and equal to 200 s per site; k is the Boltzmann constant and T is the temperature, set at 298 K in the current work.

$$E_{\text{sur}} = \frac{1}{2A} (E_{\text{slab}} - n_{\text{Ni}}(E_{\text{bulk Ni}} + \Delta\mu_{\text{Ni}}) - n_{\text{P}}(E_{\text{bulk P}} + \Delta\mu_{\text{P}})) \quad (1)$$

$$3\Delta\mu_{\text{Ni}} + \Delta\mu_{\text{P}} = E_{\text{Form Ni}_3\text{P}} = -1.78 \quad (2)$$

$$E_{\text{sur}} = \frac{1}{2A} \left(E_{\text{slab}} - n_{\text{Ni}}E_{\text{bulk Ni}} - n_{\text{P}}E_{\text{bulk P}} + \frac{1.78}{3}n_{\text{Ni}} + \Delta\mu_{\text{P}} \left(\frac{n_{\text{Ni}}}{3} - n_{\text{P}} \right) \right), \quad (3)$$

$$\Delta G_{\text{H}} = \Delta E_{\text{H}} + \Delta E_{\text{ZPE}} - T\Delta S_{\text{H}} \quad (4)$$

$$\Delta E_{\text{H}} = E[\text{Ni}_3\text{P} + \text{H}] - E[\text{Ni}_3\text{P}] - 1/2E[\text{H}_2], \quad (5)$$

$$i_0 = -ek_0 \frac{1}{1 + \exp\left(-\frac{\Delta G_{\text{H}}^*}{kT}\right)} \quad \text{for } \Delta G_{\text{H}}^* < 0 \quad (6)$$

$$i_0 = -ek_0 \frac{1}{1 + \exp\left(-\frac{\Delta G_{\text{H}}^*}{kT}\right)} \exp\left(-\frac{\Delta G_{\text{H}}^*}{kT}\right) \quad \text{for } \Delta G_{\text{H}}^* > 0 \quad (7)$$

Conflicts of interest

The authors declare no competing financial interest.

Acknowledgements

Financial support from the Ministry of Education of Singapore (RG15/16), National Natural Science Foundation of China (No. 21676216), China Postdoctoral Science Foundation (No. 2014M550507; 2015T81046) and Innovative projects of Northwest University (YZZ17140) is gratefully acknowledged.

Notes and references

- 1 Y. Zheng, Y. Jiao, Y. Zhu, L. H. Li, Y. Han, Y. Chen, A. Du, M. Jaroniec and S. Z. Qiao, *Nat. Commun.*, 2014, **5**, 3783.
- 2 Z. Chen, D. Cummins, B. N. Reinecke, E. Clark, M. K. Sunkara and T. F. Jaramillo, *Nano Lett.*, 2011, **11**, 4168–4175.
- 3 J. Xie, H. Zhang, S. Li, R. Wang, X. Sun, M. Zhou, J. Zhou, X. W. Lou and Y. Xie, *Adv. Mater.*, 2013, **25**, 5807–5813.
- 4 D. Voiry, H. Yamaguchi, J. Li, R. Silva, D. C. Alves, T. Fujita, M. Chen, T. V. Asefa, B. Shenoy, G. Eda and M. Chhowalla, *Nat. Mater.*, 2013, **12**, 850–855.
- 5 J. Yang, D. Voiry, S. J. Ahn, D. Kang, A. Y. Kim, M. Chhowalla and H. S. Shin, *Angew. Chem., Int. Ed.*, 2013, **52**, 13751–13754.
- 6 W. F. Chen, C. H. Wang, K. Sasaki, N. Marinkovic, W. Xu, J. T. Muckerman, Y. Zhu and R. R. Adzic, *Energy Environ. Sci.*, 2013, **6**, 943–951.
- 7 W. F. Chen, S. Iyer, S. Iyer, K. Sasaki, C. H. Wang, Y. M. Zhu, J. T. Muckerman and E. Fujita, *Energy Environ. Sci.*, 2013, **6**, 1818–1826.
- 8 H. Vrubel and X. L. Hu, *Angew. Chem., Int. Ed.*, 2012, **51**, 12703–12706.
- 9 B. F. Cao, C. M. Veith, J. C. Neuefeind, R. R. Adzic and P. G. Khalifah, *J. Am. Chem. Soc.*, 2013, **135**, 19186–19192.
- 10 P. Clark, W. Li and S. T. Oyama, *J. Catal.*, 2001, **200**, 140–147.
- 11 S. T. Oyama, P. Clark, V. L. S. T. Silva, E. J. Ledes and F. G. Requejo, *J. Phys. Chem. B*, 2001, **105**, 4961–4966.

- 12 M. V. Gerasimov and Y. N. Simirskii, *Metallurgist*, 2008, **52**, 477–481.
- 13 Z. Huang, Z. Chen, Z. Chen, C. Lv, H. Meng and C. Zhang, *ACS Nano*, 2014, **8**, 8121–8129.
- 14 P. Jiang, Q. Liu and X. P. Sun, *Nanoscale*, 2014, **6**, 13440–13445.
- 15 E. J. Popczun, J. R. McKone, C. G. Read, A. J. Biacchi, A. Wiltrout, M. N. S. Lewis and R. E. Schaak, *J. Am. Chem. Soc.*, 2013, **135**, 9267–9270.
- 16 L. G. Feng, H. Vrubel, M. Bensimon and X. L. Hu, *Phys. Chem. Chem. Phys.*, 2014, **16**, 5917–5921.
- 17 Y. Shu, Y. K. Lee and S. T. Oyama, *J. Catal.*, 2005, **236**, 112–121.
- 18 Y. Pan, Y. Liu, J. Zhao, K. Yang, J. Liang, D. Liu, W. Hu, D. Liu, Y. Liu and C. Liu, *J. Mater. Chem. A*, 2015, **3**, 1656–1665.
- 19 H. Zhao, S. T. Oyama, H. J. Freund, R. Włodarczyk and M. Sierka, *Appl. Catal., B*, 2015, **164**, 204–216.
- 20 K. G. Keong, W. Sha and S. Malinov, *J. Alloys Compd.*, 2002, **334**, 192–199.
- 21 M. Saitou, Y. Okudaira and W. Oshikawa, *J. Electrochem. Soc.*, 2003, **150**, C140–C143.
- 22 H. Pfeiffer, F. Tancrét, M. P. Bichat, L. Monconduit, F. Favier and T. Brousse, *Electrochem. Commun.*, 2004, **6**, 263–267.
- 23 L. Zhou, Y. Kong, Y. Du, J. Wang and Y. Zhou, *Appl. Surf. Sci.*, 2010, **256**, 7692–7695.
- 24 R. B. Wexler, J. M. P. Martirez and A. M. Rappe, *Chem. Mater.*, 2016, **28**, 5365–5372.
- 25 J. Y. Xiang, X. L. Wang, X. H. Xia, J. Zhong and J. P. Tu, *J. Alloys Compd.*, 2011, **509**, 157–160.
- 26 L. Jin, H. Xia, Z. Huang, C. Lv, J. Wang, M. G. Humphrey and C. Zhang, *J. Mater. Chem. A*, 2016, **4**, 10925–10932.
- 27 J. Pan, G. Liu, G. Q. Lu and H. M. Cheng, *Angew. Chem., Int. Ed.*, 2011, **50**, 2133–2137.
- 28 J. Hermann, M. Trachta, P. Nachtigall and O. Bludsky, *Catal. Today*, 2014, **227**, 2–8.
- 29 J. N. Wilson and H. Idriss, *J. Am. Chem. Soc.*, 2002, **124**, 11284–11285.
- 30 H. G. Yang, C. H. Sun, S. Z. Qiao, J. Zou, G. Liu, S. C. Smith, H. M. Cheng and G. Q. Lu, *Nature*, 2008, **453**, 638–642.
- 31 J. Zhu, F. Fan, R. Chen, H. An, Z. Feng and C. Li, *Angew. Chem.*, 2015, **127**, 9239–9242.
- 32 T. Takashi, O. Tomoya and K. Yasuhiro, *ACS Catal.*, 2016, **6**, 2250–2256.
- 33 J. He, M. G. Ángel, O. Bludská and P. Nachtigall, *CrystEngComm*, 2016, **18**, 3808–3818.
- 34 K. Reuter and M. Scheffler, *Phys. Rev. B: Condens. Matter Mater. Phys.*, 2001, **65**, 035406.
- 35 M. E. Schlesinger, *Chem. Rev.*, 2002, **102**, 4267–4301.
- 36 T. B. Massalski, *Binary Alloy Phase Diagrams*, ASM international, Ohio, 1990, vol. 3.
- 37 J. W. Jang, P. G. Kim and K. N. Tua, *J. Appl. Phys.*, 1999, **85**, 8456–8463.
- 38 P. Hui, *Nanoscale Res. Lett.*, 2016, **11**, 113–118.
- 39 P. Liu and J. A. Rodriguez, *J. Am. Chem. Soc.*, 2005, **127**, 14871–14878.
- 40 B. Hinnemann, P. G. Moses, J. Bonde, K. P. Jørgensen, J. H. Nielsen, S. Hørch, I. Chorkendorff and J. K. Nørskov, *J. Am. Chem. Soc.*, 2005, **127**, 5308–5309.
- 41 Y. Zheng, Y. Jiao, Y. H. Zhu, L. H. Li, Y. Han, Y. Chen, A. J. Du, M. S. Jaroniec and Z. Qiao, *Nat. Commun.*, 2014, **5**, 3783.
- 42 J. K. Nørskov, T. Bligaard, A. Logadottir, J. R. Kitchin, J. G. Chen, S. Pandalov and U. Stimming, *J. Electrochem. Soc.*, 2005, **152**, J23–J26.
- 43 T. L. Tan, L. L. Wang, D. D. Johnson and K. Bai, *J. Phys. Chem. C*, 2013, **117**, 22696–22704.
- 44 W. S. Zhi, K. Jakob, F. D. Colin, C. Ib, K. N. Jens and F. J. Thomas, *Science*, 2017, **355**, eaad4998.
- 45 Z. Q. Huang, B. Long and C. R. Chang, *Catal. Sci. Technol.*, 2015, **5**, 2935–2944.
- 46 M. T. Francesca, K. C. Jason, K. Viktoria, T. M. Matthew, Y. Jie, M. L. David, J. B. Nicholas, A. Christine, W. B. Jeffrey, M. Y. Kin, Y. Jinhui, C. Le, R. S. Matthew, S. Joshua, A. H. Frances, A. P. Kristin and D. S. Ian, *Nat. Commun.*, 2016, **7**, 12012.
- 47 J. Hu, X. Zhao, W. Chen, H. Su and Z. Chen, *J. Phys. Chem. C*, 2017, **121**, 18702–18709.
- 48 Q. Tang and D. Jiang, *ACS Catal.*, 2016, **6**, 4953–4961.